ChemComm

COMMUNICATION

View Article Online
View Journal

Cite this: DOI: 10.1039/d5cc05272f

Received 12th September 2025,
Accepted 4th November 2025

DOI: 10.1039/d5cc05272f

rsc.li/chemcomm

Detecting impurity-specific effects on structure and radiolytic hydrogen production in aluminum hydroxide

Trent R. Graham, *[a] Khashayar Ghandi, [b] Micah Prange, [a] Gregory Schenter, [a] Larry M. Anovitz, [d] Jay A. LaVerne [c] and Carolyn I. Pearce [ae]

While radiolytic hydrogen (H_2) generation is an intrinsic property of aqueous and mineral radiolysis in nuclear waste systems, detection of the sub-ns events leading to H_2 generation is challenging. Interfacial processes involving key mineral phases in the sludge, *e.g.*, gibbsite (α-$Al(OH)_3$), have been implicated, with impurities affecting the amount of H_2 generated. To understand why gibbsite synthesized from nitrate precursors produces less H_2 than gibbsite from chloride precursors, we paired ^{27}Al multiple quantum magic angle spinning (MQMAS) NMR spectroscopy to determine structural heterogeneity with transverse-field muon spin rotation (TF-μSR) to probe electron availability. MQMAS revealed greater structural disorder in the gibbsite synthesized with nitrate (NO_3-gibbsite). Correspondingly, TF-μSR showed a larger diamagnetic fraction for NO_3-gibbsite, indicating reduced persistence of μ^+-electron bound states (muonium or other radicals) and thus fewer electrons available for reaction on the sub-ns timescale. This establishes a correlation between impurity-induced disorder and electron loss. The diamagnetic fraction serves as a signature for these sub-ns events, as it provides a key constraint for predictive models without currently resolving whether the electron is lost to direct chemical scavenging or trapping at lattice defects.

The radiolytic generation of H_2 gas within nuclear waste tanks and in deep geological repositories is an intrinsic property of aqueous and mineral radiolysis. In waste tanks it requires costly infrastructure for detection, monitoring, and venting to mitigate the persistent risk of flammable gas accumulation.[1] This further complicates nuclear waste processing and long-term nuclear waste storage strategies.[2] Because gibbsite (α-$Al(OH)_3$) is a major mineral constituent of this legacy waste,[3] it provides an essential model system for understanding the fundamental solid-state pathways of H_2 generation *via* radiolysis.[1] However, the earliest steps of this process, particularly the fate of radiation-generated electrons, remain poorly resolved. A predictive understanding of how the gibbsite lattice, and any impurities within, govern this initial regime will inform management of H_2 formation and mitigation strategies.

The significance of this knowledge gap is evident in the impurity-dependent radiolysis of gibbsite. Under gamma (γ)-radiolysis, gibbsite synthesized from chloride precursors (Cl-gibbsite) produces order-of-magnitude larger H_2 yields than gibbsite synthesized from nitrate precursors (NO_3-gibbsite) with impurities present in <1 atom% amounts.[4] This dramatic difference in reactivity occurs even though bulk structural probes like X-ray diffraction, FTIR spectroscopy, and microscopy show no significant differences in the gibbsite.[1,5,6] Information regarding phenomena underlying the larger H_2 yields has been obtained by electron paramagnetic resonance (EPR) studies that identified trapped atomic hydrogen centers ($H^\bullet$) in Cl-gibbsite but not in NO_3-gibbsite.[5] Recent work has further shown that transition-metal dopants such as Fe(III) and Cr(III) also suppress $H^\bullet$ formation and reduce H_2 yields, consistent with electron scavenging mechanisms.[7] We hypothesize that the disparity in H_2 yield originates from differences in the availability or localization of precursor electrons on the sub-ns timescale. The sub-ns events in this dynamic regime are inaccessible to conventional static measurements, and while pulse radiolysis with EPR is valuable for radical detection in solutions,[8] it is not readily applicable to opaque solids such as gibbsite without specialized adaptations.

To overcome these barriers, we employed a strategy that pairs two complementary techniques. First, transverse-field muon spin rotation (TF-μSR) provides an internal, non-optical probe of electron availability at sub-ns timescale, with relaxation dynamics extending into the μs regime.[9–12] For an introduction to this technique, see Hillier *et al.*[11] In this technique,

[a] *Pacific Northwest National Laboratory, Richland, Washington 99354, USA. E-mail: trent.graham@pnnl.gov*
[b] *University of Guelph, Guelph, ON N1G 2W1, Canada*
[c] *Radiation Laboratory and Department of Physics and Astronomy, University of Notre Dame, Notre Dame, 46556, USA*
[d] *Oak Ridge National Laboratory, Oak Ridge, TN 37831, USA*
[e] *Department of Crop and Soil Sciences, Washington State University, Pullman, 99163, USA*

an implanted positive muon (μ^+) acts as a light, radioactive isotope of hydrogen possessing spin $\frac{1}{2}$ properties.[12] Implantation leads to a localized ionization track, generating a path of electron–hole pairs in a manner analogous to the primary interaction of a gamma photon.[13] The product of μ^+ implantation can yield a diamagnetic species or, if an electron is captured, a bound μ^+-electron state (muonium or other muonated radicals).[9] Upon decay, the μ^+ emits a positron that is preferentially emitted along the muon spin direction. Therefore, the relative balance between diamagnetic and paramagnetic channels provides a signature of the survival of radiation-generated electrons, because the relative magnitude of the observed diamagnetic fraction indicates the availability of radiation-generated electrons that persist before trapping or recombination.[13] This technique is paired with ^{27}Al multiple-quantum magic-angle spinning NMR (MQMAS) to characterize structural heterogeneity.[14] By resolving the distribution of local electric-field gradients around aluminum sites, MQMAS provides a bulk measure of impurity-driven disorder, where broader spectral features indicate greater structural heterogeneity.[15]

Here, we apply this combined MQMAS and μSR approach to test the central hypothesis that impurity-associated lattice disorder in gibbsite correlates directly with reduced sub-ns electron survival. We analyze the static structural features from NMR with the dynamic electronic information from TF-μSR, to establish a correlation between disorder and electron fate. These experimental results provide input for constraining predictive models of radiolysis and can be used to further develop frameworks for understanding impurity effects in other complex hydroxide and oxide materials relevant to nuclear waste management and radiation science.[10] Detailed experimental methods are available in the SI.

To investigate whether the distinct radiolytic behavior of Cl-gibbsite and NO_3-gibbsite corresponds to different structural perturbations, we first evaluated the local aluminum environments using solid-state ^{27}Al MQMAS NMR. This technique is well-suited for this purpose, as it improves spectral resolution by correlating the isotropic chemical shift with the second-order quadrupolar interaction, effectively separating the broad line shapes common to half-integer quadrupolar nuclei like ^{27}Al into a second spectral dimension.[16] In well-ordered gibbsite, the two distinct octahedral Al environments are typically resolvable in ^{27}Al MQMAS spectra.[15,17] As shown in Fig. 1, the introduction of an anionic impurity perturbs this crystalline order. Cl-gibbsite and NO_3-gibbsite nanoplatelets exhibit disparate and significantly broader spectra relative to literature studies of highly crystalline gibbsite,[15,17] indicating that both impurities increase the heterogeneity and distribution of local Al environments.

When comparing the two impurity-containing systems in Fig. 1, the Cl–gibbsite retains relatively sharper, partially resolved features, which is consistent with a more constrained or regular distribution of lattice perturbations. By contrast, the spectrum of the NO_3-gibbsite is markedly broader and less resolved. This signifies a wider distribution of electric-field gradients and thus greater structural heterogeneity throughout

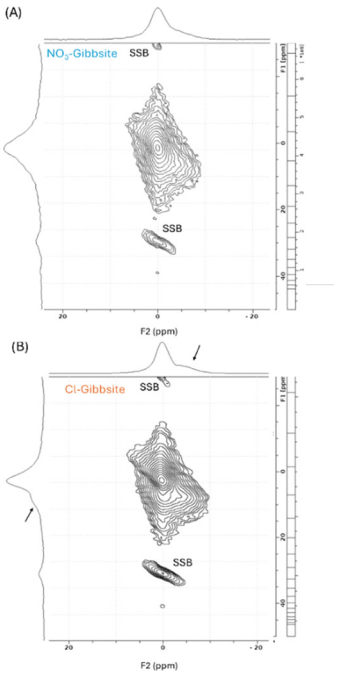

Fig. 1 ^{27}Al MQMAS NMR measure of disorder. The (A) NO_3-gibbsite and (B) Cl-gibbsite spectra. The two peaks of gibbsite are better resolved in the chloride analogue. Spinning sidebands are marked (SSB). The sharper site distribution of the Cl-gibbsite sample is annotated with an arrow.

the material.[15] A precise deconvolution of these overlapping line shapes is challenging, since either Gaussian or Lorentzian broadening of the typical site-specific parameters in gibbsite (quadrupolar coupling constant, isotropic chemical shift, and asymmetry parameter),[18] or the introduction of Czjzek-type distributions[19] can reproduce the data. However, the qualitative trend in Fig. 1 is unambiguous. This observation of greater lattice disorder in NO_3-gibbsite provides the structural context for interpreting the TF-μSR results that follow, allowing us to test whether this increased heterogeneity correlates with a change in sub-ns electron availability.

Having established a difference in structural disorder, we next used TF-μSR to probe the dynamics of radiation-induced electrons for ps to sub-ns timescale. In this experiment, the observed implanted μ^+ may follow one of three outcomes: (i) appear as a long-lived diamagnetic species, (ii) form persistent paramagnetic μ^+-electron states (Mu or other muoniated radicals with a life time from 0.1 μs to potentially several μs), or (iii) undergo ultrafast loss ($<$few ns but longer than 100 ps) of Mu radicals^{-1} that depolarize too rapidly to be resolved. The present data do not allow quantitative partitioning between (ii) and (iii), but both contribute to the sub-ns asymmetry loss distinguished from the well-defined diamagnetic fraction. The relative abundance of these states is quantified from their amplitude in the TF-μSR data. The amplitude of the diamagnetic fraction (A_{dia}) serves as a direct, inverse proxy for electron availability at the muon's stopping site. A larger A_{dia} signifies suppressed formation of (ii) and (iii) and thus reduced electron availability.

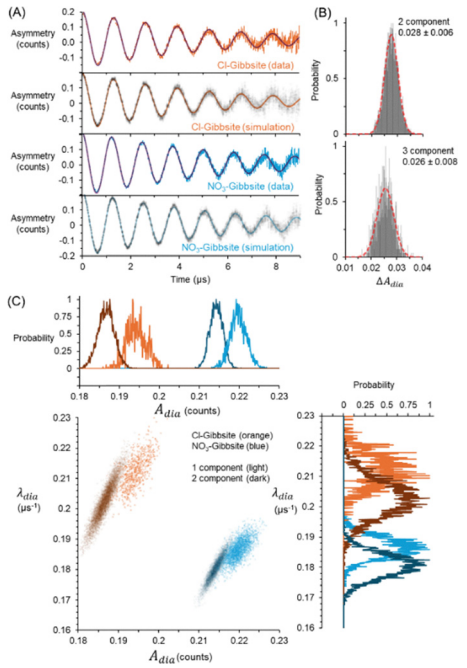

Fig. 2 TF-μSR diamagnetic fraction and model consistent ΔA_{dia}. (A) Data and traditional NLLS fit (black line) and representative ensemble fits (0–10 μs) for Cl-gibbsite (top) and NO_3-gibbsite (bottom) with MC-UQ bands, showing reliable capture of the long-lived component. (B) ΔA_{dia} for each model with Lorentzian fits. (C) Joint posteriors for A_{dia} and λ_{dia}.

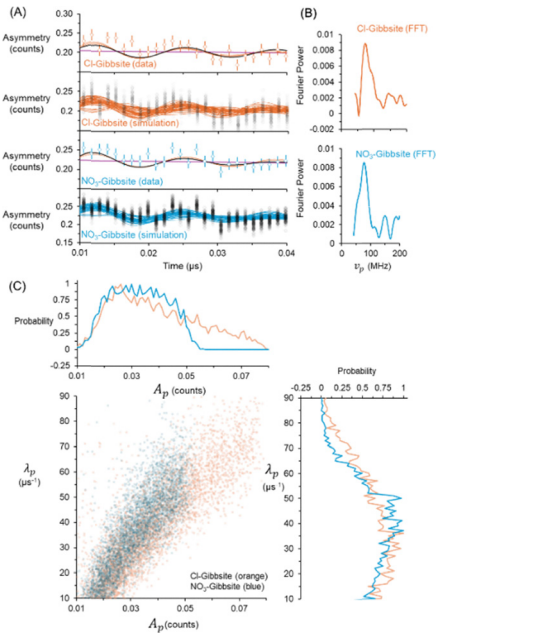

Fig. 3 TF-μSR analysis of fast components. (A) Short-time projection (<0.08 μs) showing that the two-component model (purple) underpredicts early data (<0.01 μs). The traditional NLLS fit is shown in black, while fixed-λ fits (red, 60–20 μs^{-1}) overlay each other, indicating parameter unidentifiability. (B) Fourier transform magnitude shows a weak ~80 MHz feature assigned to a paramagnetic species in both samples. (C) Joint posteriors for A_p and λ_p (μs^{-1}) confirm poor identifiability, with amplitudes bounded to $\leq$0.05 (NO_3) and $\leq$0.08 (Cl), importantly leaving the difference in A_{dia} (Fig. 2) unchanged.

Our central finding is that nitrate and chloride impurities result in disparate A_{dia} in gibbsite. As shown in Fig. 2A, both a 2-component model (diamagnetic oscillator + constant background, treating the ~0.1 μs asymmetry as lost) and a 3-component model (diamagnetic + fast paramagnetic oscillator + constant background, explicitly assigning part of the ~0.1 μs signal to a short-lived μ^+-electron state) fit the long-lived diamagnetic precession envelope in both samples, establishing model adequacy for extracting A_{dia}. Fig. 2B shows that NO_3-gibbsite exhibits a larger A_{dia} than Cl-gibbsite, independent of the inclusion of an additional component attributable to a free radical. This result provides evidence that sub-ns electron availability is diminished in the more disordered, NO_3-gibbsite. Reported values, such as those in Fig. 2B for the 2 and 3 component models, were primarily determined *via* Monte Carlo Uncertainty Quantification (MC-UQ) as detailed in the SI. This approach, which resamples variance-matched synthetic datasets, accounts for non-linear parameter correlations.[20] The joint posteriors in Fig. 2C show that the regions of solution of A_{dia} and λ_{dia} are well constrained and exhibit weak correlation, supporting the reliability of A_{dia} as an independent parameter not convoluted with other parameters, unlike the poorly identifiable paramagnetic fraction (A_p) parameters described hereafter.

To test the sensitivity of our results to model choice, we compared a two-component fit and three-component fit at $t <$ 0.04 μs. As shown in Fig. 3A, the two-component model systematically underpredicts the initial asymmetry at $t <$ 0.01 μs, indicating an unresolved fast-decaying contribution. Fourier-transform inspection of the ns asymmetry (0–0.01 μs) in Fig. 3B reveals a weak feature at ~80 MHz (≈ 60 G) in both samples, consistent with a short-lived paramagnetic state. Incorporating this contribution in the three-component model reduces the residuals, but the fast-term parameters, such as A_p, remain poorly identifiable. Posterior distributions in Fig. 3C show this weak identifiability as a ridge of solutions, bounding A_p to $\leq$0.05 in nitrate and $\leq$0.08 in chloride. ΔA_{dia} is invariant across both models and links the greater structural disorder observed by NMR (Fig. 1) to suppressed electron survival on the sub-ns timescale.

We note the minor difference in applied fields (≈58.3 G *vs.* 56.1 G) affects the precession frequency but has a negligible impact on A_{dia} in this regime.[21] Interpretation of secondary parameters, such as the diamagnetic relaxation rate and frequency, as well as the bounded properties of the short-lived component (SI), will require future experiments varying temperature and field strength. Definitive species-level assignment of short-lived paramagnetic components will require measuring the hyperfine coupling constant along with simulations, which are not included in the present work but are planned for follow-up studies.

Taken together, the combined MQMAS NMR and TF-μSR measurements provide an opportunity to further constrain mechanisms of impurity effects in gibbsite. The ^{27}Al MQMAS results (Fig. 1) unambiguously show that nitrate impurities

induce a broader dispersion of local aluminum environments than chloride, signifying greater structural heterogeneity. Complementing this structural observation, the TF-μSR results (Fig. 2 and 3) reveal that this NO_3-gibbsite exhibits a larger diamagnetic fraction following μ^+ implantation.

Part of the sub-ns asymmetry could arise from short-lived paramagnetic μ^+-electron states (Mu or other radicals) or from ultrafast quenching processes. The current data likewise cannot distinguish between direct electron scavenging by the nitrate impurity *versus* trapping at a nitrate-induced lattice defect. Specifically, two competing (and potentially synergistic) pathways could explain our observations. The effect could be primarily chemical, where the nitrate ion acts as a direct and efficient scavenger for electrons. Alternatively, the effect could be physical, where the extensive lattice disorder itself creates structural defects that trap electrons or reduce their mobility, thus preventing them from reaching the muon.

The order-of-magnitude disparities in final H_2 yields likely also reflect downstream processes, such as defect-assisted transport and trapping, that occur beyond the timescale probed here. Within this context, the modest increase in the diamagnetic fraction for NO_3-gibbsite (ΔA_{dia} = 0.03) is directionally consistent with the absence of persistent $H^\bullet$ centers by EPR and the lower bulk H_2 yields.[4] While this study is limited to a point comparison of gibbsite with trace chloride or nitrate, it is nevertheless consistent with a reduced electron availability for bound-state formation in the nitrate-containing material. Our TF-μSR measurements therefore provide a sub-ns mechanistic complement to these longer-timescale probes. More broadly, quantifying impurity-induced changes in A_{dia}, coupled with future refinements in resolving the abundance and properties of the short-lived μ^+-electron states, offers a strategy for interrogating how impurities modulate radiolysis across diverse oxide and hydroxide systems.

This research was supported by IDREAM (Ion Dynamics in Radioactive Environments and Materials), an Energy Frontier Research Center funded by the U.S. Department of Energy (DOE), Office of Science, Basic Energy Science (BES) under FWP 68932. PNNL is a multiprogram national laboratory operated for DOE by Battelle Memorial Institute, operating under Contract No. DE AC05-76RL0-1830. Support for K. Ghandi was provided by the Natural Sciences and Engineering Research Council of Canada (NSERC), and he was the awardee of the beamtime. NSERC also funded travel to TRIUMF for Cody Landry and Nicholas Oudejans, who are thanked for assistance collecting the data. A large language model assisted with language editing. We gratefully acknowledge the personnel of the Centre for Molecular and Materials Science at TRIUMF for their assistance.

Conflicts of interest

There are no conflicts to declare.

Data availability

Data supporting this article have been included as part of the supplementary information (SI). Supplementary information: Cl-gibbsite and NO_3-gibbsite synthesis conditions, methods for ^{27}Al MQMAS NMR and TF-μSR, Monte Carlo Uncertainty Quantification procedure, and tabulated results. See DOI: **https://doi.org/10.1039/d5cc05272f**.

Notes and references

1 J. A. Kaddissy, S. Esnouf, D. Durand, D. Saffre, E. Foy and J.-P. Renault, *J. Phys. Chem. C*, 2017, **121**, 6365–6373.
2 R. A. Peterson, E. C. Buck, J. Chun, R. C. Daniel, D. L. Herting, E. S. Ilton, G. J. Lumetta and S. B. Clark, *Environ. Sci. Technol.*, 2018, **52**, 381–396.
3 A. Westesen and R. Peterson, *Environ. Prog. Sustainable Energy*, 2022, **41**, e13789.
4 H. Hlushko, A. Ramos-Ballesteros, P. Chen, X. Zhang, K. M. Rosso, C. I. Pearce and J. A. LaVerne, *Phys. Chem. Chem. Phys.*, 2024, **26**, 9867–9870.
5 E. Briley, P. Huestis, X. Zhang, K. M. Rosso and J. A. LaVerne, *Mater. Chem. Phys.*, 2021, **271**, 124885.
6 P. L. Huestis, T. R. Graham, S. T. Mergelsberg and J. A. LaVerne, *Thermochim. Acta*, 2020, **689**, 178611.
7 H. Hlushko, A. Ramos-Ballesteros, A. Bedar, P. Chen, X. Zhang, R. Colina Ruiz, K. M. Rosso, C. Pearce and J. A. LaVerne, *J. Phys. Chem. C*, 2025, **129**, 16927–16937.
8 M. Daniels, *J. Phys. Chem.*, 1969, **73**, 3710–3717.
9 C. J. Rhodes, *Sci. Prog.*, 2012, **95**, 101–174.
10 K. Ghandi, C. Landry, T. Du, M. Lainé, A. Saul and S. Le Caër, *Sci. Rep.*, 2019, **9**, 17165.
11 A. D. Hillier, S. J. Blundell, I. McKenzie, I. Umegaki, L. Shu, J. A. Wright, T. Prokscha, F. Bert, K. Shimomura, A. Berlie, H. Alberto and I. Watanabe, *Nat. Rev. Methods Primers*, 2022, **2**, 4.
12 S. J. Blundell, *Chem. Rev.*, 2004, **104**, 5717–5736.
13 C. Landry, A. H. E. Morrison and K. Ghandi, *Radiat. Phys. Chem.*, 2020, **173**, 108881.
14 J. Kanellopoulos, D. Freude and A. Kentgens, *Solid State Nucl. Magn*, 2007, **32**, 99–108.
15 C. V. Chandran, C. E. A. Kirschhock, S. Radhakrishnan, F. Taulelle, J. A. Martens and E. Breynaert, *Chem. Soc. Rev.*, 2019, **48**, 134–156.
16 A. Medek, J. S. Harwood and L. Frydman, *J. Am. Chem. Soc.*, 1995, **117**, 12779–12787.
17 S. E. Ashbrook, J. McManus, K. J. D. MacKenzie and S. Wimperis, *J. Phys. Chem. B*, 2000, **104**, 6408–6416.
18 S. Xu, N. R. Jaegers, W. Hu, J. H. Kwak, X. Bao, J. Sun, Y. Wang and J. Z. Hu, *ACS Omega*, 2021, **6**, 4090–4099.
19 J. B. d'Espinose de Lacaillerie, C. Fretigny and D. Massiot, *J. Magn. Reson.*, 2008, **192**, 244–251.
20 M. T. Martins and F. R. Lourenço, *Anal. Chim. Acta*, 2024, **1330**, 343285.
21 T. Junginger, R. Laxdal, W. A. MacFarlane and A. Suter, *Front. Electron. Mater.*, 2024, **4**, 1–18.